

Measuring aberrations in the rat brain by coherence-gated wavefront sensing using a Linnik interferometer

Jinyu Wang,^{1,2,3,4,5} Jean-François Léger,^{1,2,3} Jonas Binding,^{1,2,3,4,5,6} A. Claude Boccara,⁴ Sylvain Gigan,^{4,*} and Laurent Bourdieu^{1,2,3}

¹Ecole Normale Supérieure, Institut de Biologie de l'ENS, IBENS, Paris, F-75005 France

²Inserm, U1024, Paris F-75005 France

³CNRS, UMR 8197, Paris, F-75005 France

⁴Institut Langevin, ESPCI ParisTech, CNRS UMR 7587, ESPCI, 1 rue Jussieu, 75005 Paris, France

⁵Fondation Pierre-Gilles de Gennes pour la Recherche, 29 rue d'Ulm, Paris, 75005 France

⁶Max Planck Institute for Medical Research, Jahnstraße 29, Heidelberg, 69120 Germany

*sylvain.gigan@espci.fr

Abstract: Aberrations limit the resolution, signal intensity and achievable imaging depth in microscopy. Coherence-gated wavefront sensing (CGWS) allows the fast measurement of aberrations in scattering samples and therefore the implementation of adaptive corrections. However, CGWS has been demonstrated so far only in weakly scattering samples. We designed a new CGWS scheme based on a Linnik interferometer and a SLED light source, which is able to compensate dispersion automatically and can be implemented on any microscope. In the highly scattering rat brain tissue, where multiply scattered photons falling within the temporal gate of the CGWS can no longer be neglected, we have measured known defocus and spherical aberrations up to a depth of 400 μm .

© 2012 Optical Society of America

OCIS codes: (110.1080) Active or adaptive optics; (010.7350) Wave-front sensing; (110.0113) Imaging through turbid media.

References and links

1. O. Albert, L. Sherman, G. Mourou, T. B. Norris, and G. Vdovin, "Smart microscope: an adaptive optics learning system for aberration correction in multiphoton confocal microscopy," *Opt. Lett.* **25**(1), 52–54 (2000).
2. P. Marsh, D. Burns, and J. Girkin, "Practical implementation of adaptive optics in multiphoton microscopy," *Opt. Express* **11**(10), 1123–1130 (2003).
3. M. J. Booth, M. A. Neil, and T. Wilson, "New modal wave-front sensor: application to adaptive confocal fluorescence microscopy and two-photon excitation fluorescence microscopy," *J. Opt. Soc. Am. A* **19**(10), 2112–2120 (2002).
4. M. J. Booth, M. A. Neil, R. Juskaitis, and T. Wilson, "Adaptive aberration correction in a confocal microscope," *Proc. Natl. Acad. Sci. U.S.A.* **99**(9), 5788–5792 (2002).
5. D. Débarre, E. J. Botcherby, M. J. Booth, and T. Wilson, "Adaptive optics for structured illumination microscopy," *Opt. Express* **16**(13), 9290–9305 (2008).
6. D. Débarre, E. J. Botcherby, T. Watanabe, S. Srinivas, M. J. Booth, and T. Wilson, "Image-based adaptive optics for two-photon microscopy," *Opt. Lett.* **34**(16), 2495–2497 (2009).
7. N. Ji, D. E. Milkie, and E. Betzig, "Adaptive optics via pupil segmentation for high-resolution imaging in biological tissues," *Nat. Methods* **7**(2), 141–147 (2010).
8. N. Ji, T. R. Sato, and E. Betzig, "Characterization and adaptive optical correction of aberrations during in vivo imaging in the mouse cortex," *Proc. Natl. Acad. Sci. U.S.A.* **109**(1), 22–27 (2012).
9. B. M. Hanser, M. G. Gustafsson, D. A. Agard, and J. W. Sedat, "Phase-retrieved pupil functions in wide-field fluorescence microscopy," *J. Microsc.* **216**(1), 32–48 (2004).
10. M. Rueckel and W. Denk, "Properties of coherence-gated wavefront sensing," *J. Opt. Soc. Am. A* **24**(11), 3517–3529 (2007).
11. M. Rueckel, J. A. Mack-Bucher, and W. Denk, "Adaptive wavefront correction in two-photon microscopy using coherence-gated wavefront sensing," *Proc. Natl. Acad. Sci. U.S.A.* **103**(46), 17137–17142 (2006).
12. M. Feierabend, M. Rückel, and W. Denk, "Coherence-gated wave-front sensing in strongly scattering samples," *Opt. Lett.* **29**(19), 2255–2257 (2004).

13. H. Schreiber and J. H. Bruning, "Phase shifting interferometry," in *Optical Shop Testing*, 3rd ed., D. Malacara, ed. (Wiley-Interscience, Hoboken, NJ, 2007), pp. 547–667.
14. S. Tuohy and A. G. Podoleanu, "Depth-resolved wavefront aberrations using a coherence-gated Shack-Hartmann wavefront sensor," *Opt. Express* **18**(4), 3458–3476 (2010).
15. J. Wang, J.-F. Leger, J. Binding, C. Boccara, S. Gigan, and L. Bourdieu, "Measuring aberrations in the rat brain by a new coherence-gated wavefront sensor using a Linnik interferometer," *Proc. SPIE* **8227**, 822702, 822702-7 (2012).
16. J. Wang, J.-F. Léger, J. Binding, C. Boccara, S. Gigan, and L. Bourdieu, "Measuring known aberrations in rat brain slices with Coherence-Gated Wavefront Sensor based on a Linnik interferometer," in *Biomedical Optics*, OSA Technical Digest (Optical Society of America, 2012), BTu3A.83.
17. J. Binding, J. Ben Arous, J. F. Léger, S. Gigan, C. Boccara, and L. Bourdieu, "Brain refractive index measured in vivo with high-NA defocus-corrected full-field OCT and consequences for two-photon microscopy," *Opt. Express* **19**(6), 4833–4847 (2011).
18. R. Crane, "Interference phase measurement," *Appl. Opt.* **8**, 538–542 (1969).
19. D. C. Ghiglia, G. A. Mastin, and L. A. Romero, "Cellular-automata method for phase unwrapping," *J. Opt. Soc. Am. A* **4**(1), 267–280 (1987).
20. R. Gens, "Two-dimensional phase unwrapping for radar interferometry: developments and new challenges," *Int. J. Remote Sens.* **24**(4), 703–710 (2003).
21. R. J. Noll, "Zernike polynomials and atmospheric turbulence," *J. Opt. Soc. Am.* **66**(3), 207–211 (1976).
22. A. V. Larichev, P. V. Ivanov, I. G. Iroshnikov, and V. I. Shmal'gauzen, "Measurement of eye aberrations in a speckle field," *Quantum Electron.* **31**(12), 1108–1112 (2001).
23. A. V. Koryabin, V. I. Polezhaev, and V. I. Shmal'gauzen, "Measurement of the thermo-optic aberrations of active elements based on yttrium aluminate and garnet," *Quantum Electron.* **23**(10), 899–901 (1993).
24. M. Rückel, "Adaptive wavefront correction in two-photon microscopy using coherence-gated wavefront sensing," Ph.D. thesis (Ruperto-Carola University of Heidelberg, 2006).
25. Y. Piedrière, J. Cariou, Y. Guern, B. Le Jeune, G. Le Brun, and J. Lortrian, "Scattering through fluids: speckle size measurement and Monte Carlo simulations close to and into the multiple scattering," *Opt. Express* **12**(1), 176–188 (2004).
26. T. R. Hillman, Y. Choi, N. Lue, Y. Sung, R. R. Dasari, W. Choi, and Z. Yaqoob, "A reflection-mode configuration for enhanced light delivery through turbidity," *Proc. SPIE* **8227**, 82271T, 82271T-6 (2012).
27. J. W. Goodman, "Some fundamental properties of speckle," *J. Opt. Soc. Am.* **66**(11), 1145–1150 (1976).
28. J. Mertz, *Introduction to Optical Microscopy* (Roberts, Greenwood Village, CO, 2010).
29. M. Oheim, E. Beaurepaire, E. Chaigneau, J. Mertz, and S. Charpak, "Two-photon microscopy in brain tissue: parameters influencing the imaging depth," *J. Neurosci. Methods* **111**(1), 29–37 (2001).
30. D. Kleinfeld, P. P. Mitra, F. Helmchen, and W. Denk, "Fluctuations and stimulus-induced changes in blood flow observed in individual capillaries in layers 2 through 4 of rat neocortex," *Proc. Natl. Acad. Sci. U.S.A.* **95**(26), 15741–15746 (1998).
31. F. Helmchen and W. Denk, "Deep tissue two-photon microscopy," *Nat. Methods* **2**(12), 932–940 (2005).
32. C. Wang, L. Qiao, F. He, Y. Cheng, and Z. Xu, "Extension of imaging depth in two-photon fluorescence microscopy using a long-wavelength high-pulse-energy femtosecond laser source," *J. Microsc.* **243**(2), 179–183 (2011).
33. D. Kobat, N. G. Horton, and C. Xu, "In vivo two-photon microscopy to 1.6-mm depth in mouse cortex," *J. Biomed. Opt.* **16**(10), 106014 (2011).
34. G. J. Tearney, M. E. Brezinski, J. F. Southern, B. E. Bouma, M. R. Hee, and J. G. Fujimoto, "Determination of the refractive index of highly scattering human tissue by optical coherence tomography," *Opt. Lett.* **20**(21), 2258 (1995).
35. R. Juškaitis, "Characterizing high numerical aperture microscope objective lenses," in *Optical Imaging and Microscopy*, 2nd ed., P. Török and F.-J. Kao, eds. (Springer-Verlag, Berlin, 2007), pp. 21–45.
36. M. J. Booth, M. A. A. Neil, and T. Wilson, "Aberration correction for confocal imaging in refractive-index-mismatched media," *J. Microsc.* **192**(2), 90–98 (1998).
37. M. Feierabend, "Coherence-gated wave-front sensing in strongly scattering samples," Ph.D. thesis (Ruperto-Carola University of Heidelberg, 2004).
38. E. J. Botcherby, R. Juskaitytis, M. J. Booth, and T. Wilson, "An optical technique for remote focusing in microscopy," *Opt. Commun.* **281**(4), 880–887 (2008).

1. Introduction

For biological imaging applications, light microscopy always compromises between image quality, penetration and non-invasiveness. However, due to refractive index mismatch (e.g., between water and tissue for water immersion objectives) and inhomogeneity within the specimen, wavefront distortions limit signal and contrast in deep imaging, especially for confocal, multi-photon microscopy or full-field Optical Coherence Tomography (ff-OCT). With an Adaptive Optics system, the wavefront of illumination can be shaped to compensate the distortion so that a diffraction-limited focus is restored. However, a traditional Shack-

Hartmann sensor (SHS) can't be used easily in strongly scattering biological samples since there is no selection of the ballistic photons originating from the reference point at a given depth in the sample amongst all scattered photons coming from the bulk.

To avoid this pitfall, several sensorless schemes have been implemented: (i) stochastic methods based upon genetic [1] or hill-climbing algorithms [2], in which strongly stained specimens and numerous iterations are needed; (ii) model-based approaches based upon modal wavefront sensing [3], in which the reduced number of measurements minimizes photobleaching and damage to the sample and which have been demonstrated in, e.g., confocal microscopy [4], structured illumination microscopy [5] and two-photon fluorescence microscopy [6]; (iii) pupil segmentation methods [7,8]; (iv) indirect aberration measurement through phase retrieval from images [9].

In contrast, coherence-gated wavefront sensing (CGWS) [10–12], which combined low-coherence phase shifting interferometry (PSI) [13] and a real SHS or a virtual SHS (vSHS) [10–12], can measure the distortions of the wavefront in scattering samples and therefore allow their correction by adaptive optics. Aberrations can be corrected at a high temporal rate since the wavefront distortions can be obtained with a single measurement. These pioneering studies implemented CGWS in two-photon fluorescence microscopy, where a femtosecond pulsed laser was used as the low coherence light source and an appropriate amount of BK7 glass was incorporated in the reference arm for the compensation of dispersion between the two arms. CGWS has been validated in a solution of scattering beads [10,12] and up to a depth of 200 μm in the weakly scattering zebrafish forebrain [11]. Most recently, coherence gating with a real SHS has been demonstrated to reject unwanted back reflections [14] of lens surfaces far from the focus. A limit of this last approach is the difficulty to combine the sample aberrated wavefront and the reference arm wavefront. It prevents in particular using commercial SHS, since the collimated reference beam has to be recombined with the sample light behind the lenslet array in order to have interference to take place [14].

Here, we implement a new CGWS scheme based on a Linnik interferometer with a Superluminescent Light-Emitting Diode (SLED) as low-temporal-coherence light source. Compared to the previously described CGWS setup [10–12], its main advantages are the automatic compensation of dispersion between the two arms of the interferometer due to their symmetry and its possible implementation on any microscope due to its simple design [15,16]. In fresh thick highly scattering rat brain slices, for a medium range numerical-aperture (NA) and low-magnification ($20\times/0.5$) objective, we successfully measure up to a depth of about 400 μm a known defocus aberration, obtained by displacing the coherence gate (CG) position with respect to the actual focus position (AFP). With a high-NA and high-magnification ($63\times/0.9$) objective, we measure up to a depth of about 200 μm the defocus as well as the 3rd order spherical aberration introduced by the CG displacement. In contrast with the previous publications using CGWS [10–12], where backscattered light was mostly ballistic, multiple scattering is found to be not negligible in the rat brain. In addition to the ballistic photons, the CG of the SLED source also selects photons that have experienced multiple scattering, if their time of flight lies within the temporal gate. The experimental results show that the multiply scattered photons selected by the CG begin to influence the wavefront measurements at shallow depths, of the order of the mean free path. However, we show that wavefront distortions can be measured at much larger depths, despite the fact that it relies on photons originating from a diffuse Coherent Volume (dCV), which is much larger than the Coherent Volume (CV) defined by ballistic photons only. CGWS measurement eventually fails, presumably when the dCV starts to deviate too much from the CV.

List of abbreviations: NFP, nominal focus position; AFP, actual focus position; BFP, back focal plane; CG, coherence gate; CV, coherence volume; dCV, diffuse coherence volume; CGWS, coherence gated wavefront sensing; FOV, field of view; NA, numerical aperture; eNA, effective numerical aperture; OCT, optical coherence tomography; ff-OCT, full-field optical coherence tomography; PSF, point spread function; PSI, phase shifting interferometry;

SLED, superluminescent light emitting diode; SHS, Shack-Hartmann sensor; vSHS, virtual Shack-Hartman sensor.

2. Materials and methods

2.1 CGWS setup

The experimental setup (Fig. 1) used to implement CGWS is a custom-made Linnik low-coherence interferometer (a Michelson interferometer with identical objectives in each arm) [15]. Two different pairs of water immersion objectives were investigated: medium range-NA and low-magnification ($20\times/0.5$) objectives and high-NA and high-magnification ($63\times/0.9$) objectives. The low-coherence source (SLED, center wavelength 750 nm, bandwidth 23 nm) is collimated, made circularly polarized with the polarizer and the quarter wave plate, expanded to overfill the pupil of the objectives and split with a beam splitter cube (BS1). The output of the interferometer is sent to: (a) CCD2 conjugated with the object plane by L1, in order to position before each experiment the focus of the sample arm objective at the surface of the sample (the second surface of the coverslip), where the origin of the nominal focus position (NFP) is defined; (b) CCD1 conjugated with the pupil planes by the afocal telescope L1, L2; (c) a real SHS (not shown in Fig. 1) also conjugated with the pupil planes. The SHS is used for calibration and alignment of each arm individually while the pupil of the other arm is blocked. CCD1 is used to record the interference pattern of the light fields on the pupils p1 and p2. Using PSI, the wavefront topography and hence the aberrations on the pupil p1 of the sample arm are measured. A grade A cover slip (refractive index 1.51) is placed on the rat

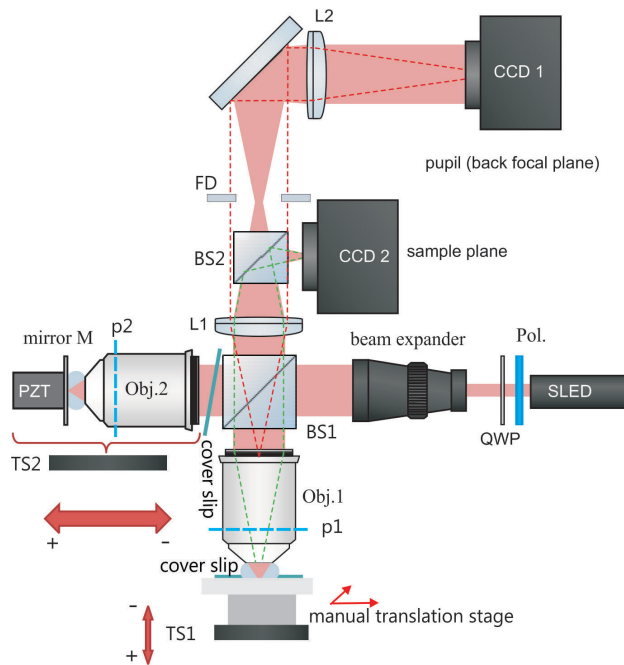


Fig. 1. Schematic of the experiment. Illumination: SLED (Superluminescent Light Emitting diode), Pol (polarizer), QWP (quarter wave plate), BS1 (beam splitter). Sample arm: Obj. 1 (microscope objective), TS1 (motorized linear translation stage allowing axial movement of the sample), coverslip (to protect the sample), 2D lateral manual translation stage. Reference arm: coverslip (to compensate dispersion from the coverslip in the sample arm), Obj. 2 (microscope objective identical to Obj. 1), M (reference mirror), PZT (piezo actuator for phase-shifting), TS2 (motorized translation stage to adjust the reference arm length). Detection: L1 and L2 (lens doublets), CCD1 and CCD2 (CCD cameras), BS1 (beam splitter), FD (adjustable field diaphragm of the microscope). The piezo, camera, TS1 and TS2 are controlled by a PC running a modified version of the Light-CT software (LLTech).

brain slice to protect it. A similar cover slip is used in the reference arm to balance the dispersion and is slightly tilted to remove unwanted back reflections. A field diaphragm is placed between the two lenses of the afocal telescope to control and tune the microscope field of view (FOV). The FOV is calibrated for different values of the FD diameter both by using geometrical optics and by measuring it with an optical fiber translated in the focal plane of the objective.

The coherence length l_c of our SLED is $21.5 \mu\text{m}$, determined from its bandwidth $\Delta\lambda$ and central wavelength λ as $0.88\lambda^2/\Delta\lambda$. It corresponds to a CG length $l_c/2n$ of $7.9 \mu\text{m}$ in the rat brain (refractive index $n = 1.36$ at 750 nm [17]). The CGWS mostly senses the light scattered within the coherence volume (CV), whose axial length (centered at CG) depends on the coherence length, which is defined by the FWHM of the self-coherence function [10].

The sample can be shifted with TS1 along the optical axis, bringing different sample layers into focus. At the surface of the sample, the focus position coincides with CG position, by alignment (Fig. 2(a)). When imaging into a sample whose refractive index n_s is greater than the index n_i of the immersion medium, refraction at the surface causes the AFP of the objective to be shifted deeper into the sample with respect to the NFP (Fig. 2(b)). Because of the index mismatch between the refractive indices of water (used for immersion in the sample arm) and of the sample, the CV simultaneously moves in the opposite direction (Fig. 2(b)) [17]. By moving TS2 (Fig. 1), we can change the CV position and therefore either compensate this effect, or create a known additional defocus as well as some spherical aberrations (Fig. 2(c)) (see Appendix A).

In our coordinate system, the AFP is taken as the origin and the positive direction points deeper into the sample. We define the CG position as the distance between the AFP and the CV center on the optical axis. Finally, as paraxial calculation is not valid for high-NA objectives, we locate the AFP with ray tracing method (see appendix A): a quasi point source of light is shifted along the optical axis and the AFP is defined as the position where the defocus aberration is zero (some higher order aberrations still remain).

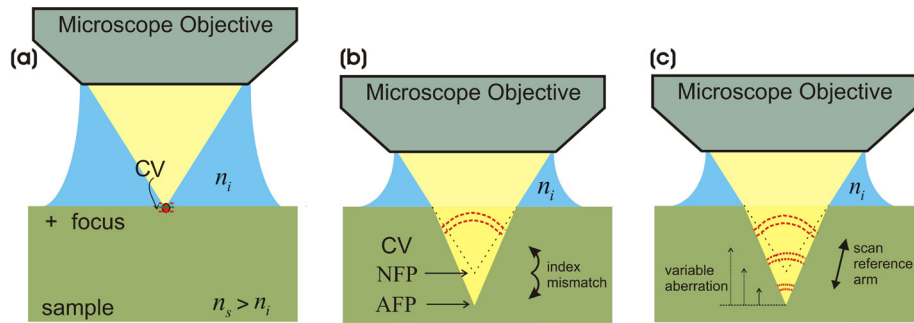


Fig. 2. Principle of the method used to create known aberration. (a) Initial state at the surface of the sample (no aberration). (b) When focusing into the sample, the index mismatch moves the CV and the AFP in opposite directions away from the NFP and introduces tractable aberrations. (c) By changing the reference arm length, the CV position can be further displaced to add or subtract aberrations.

2.2 Wavefront reconstruction

In order to extract the phase of the electric field corresponding to the CGWS-selected backscattered light on CCD1 (Fig. 1), we use four-step PSI [13,18] by shifting the mirror M mounted on the piezoelectric translation stage PZT (Fig. 1) in the reference arm. The mirror M is positioned at the focus of the objective during the alignment process using the SHS. The amplitude of the PZT is optimized to produce the optimal phase stepping of $\pi/2$. Theoretically (see appendix A), the PZT movements may introduce some defocus and high-order aberrations, but only up to a RMS wavefront error less than 1 nm for both $20\times/0.5$ and $63\times/0.9$ objectives. We therefore omit this effect in our computation. The motion of the PZT

is synchronized to the frame rate of CCD1. For each measurement, the corresponding electric field (defined as the “CGWS signal”, and whose intensity is shown in Fig. 3(b)) is extracted from a recorded quadruplet of interferograms (Fig. 3(a)) by the four-step PSI algorithm. As the maximal frame rate of CCD1 is 60 frames per second (fps), the phase can be extracted at the maximum speed of 15 fps.

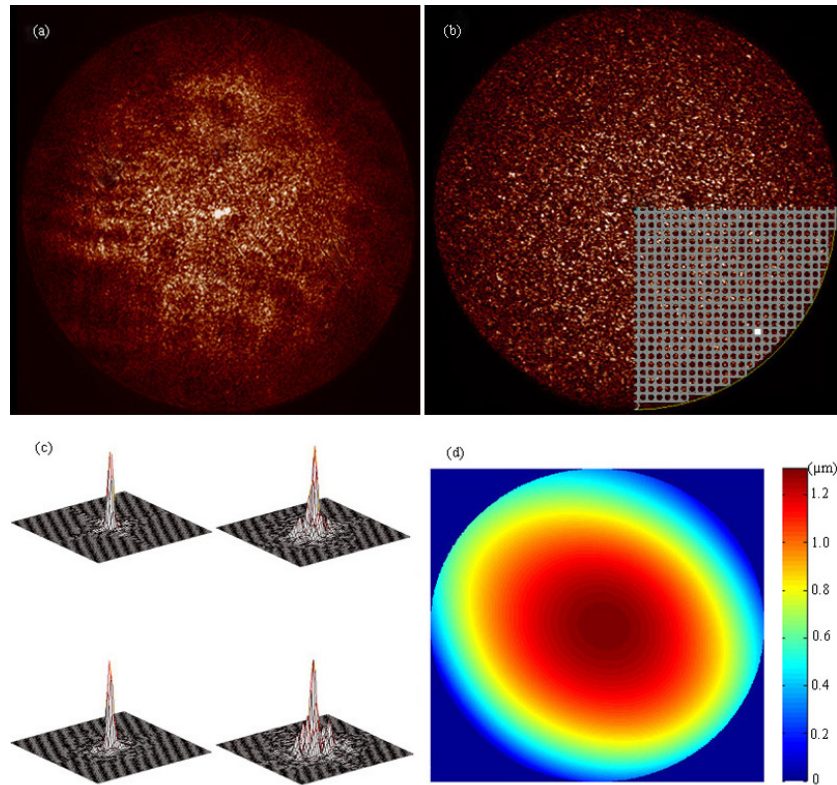


Fig. 3. Wavefront reconstruction procedure. (a) Raw image recorded on CCD1 (imaging the objective pupils), in a rat brain slice, for AFP located $160\ \mu\text{m}$ deep below the coverslip and $\text{CG} = -15\ \mu\text{m}$ from AFP ($20\times/0.5$ objective). (b) Corresponding amplitude of the electric field obtained by PSI. Bottom right corner, schematic of the virtual lens array. (c) Intensity distributions in the virtual image plane of the sublens in white of subfigure (b) obtained by discrete Fourier transform for 4 CGWS images obtained at 4 neighboring sample positions. (d) The wavefront reconstructed from the slopes of the centroids of the vSHS at a given position and then averaged over $M = 5$ neighboring positions (here corresponding to a Zernike defocus coefficient of $0.31\ \mu\text{m}$).

We use a vSHS [10,12] to unwrap the phase extracted by PSI and reconstruct the actual wavefront [15]. Though the speckle arising in scattering samples prevents the use in CGWS of traditional phase unwrapping methods, which are strongly limited by path inconsistencies due to singularities [19] and discontinuities [20], the vSHS overcomes these problems and allows reliable wavefront unwrapping in the presence of speckle [10–12,14]. The reconstruction of the wavefront was based on the algorithm implemented by Denk’s group [10,12], in terms of the first 28 Zernike modes (up to 6th radial order) [21], which we briefly summarize here. The wavefront is numerically propagated through a virtual sublens array. For this purpose, the entire aperture is divided into a number of square-shaped sublenses (Fig. 3(b)). For the $20\times/0.5$ objective, we choose a sublens size of 20 by 20 pixels (49 sublenses across the pupil). For the $63\times/0.9$ objective, the sublens size was chosen as 13 by 13 pixels (47 sublenses across the pupil). For each sublens, we perform a discrete Fourier

transformation of the electric field over its sub-aperture. With scattering samples, the amplitude distribution of the electric field on a sublens is speckled. As a consequence, the discrete Fourier transform also shows a speckle structure in the focal plane [11,22] (Fig. 3(c)). To reduce this speckle noise, we measure a number M of independent ensembles of scatters (Fig. 3(c)) [10,11]. In most experiments, we use $M = 5$ positions shifted on line with intervals of $3 \mu\text{m}$. In some experiments (see figure captions), a larger M value is used and the shifted positions are placed on a grid with $3 \mu\text{m}$ spacing. At each position, (i) a center of mass algorithm [23] is used to locate the centroid of the intensity distribution, which is preferable to other techniques [22], (ii) the slopes of the local wavefront are calculated, (iii) the wavefront (described with Zernike coefficients) is reconstructed by least-square fit to the array of local slopes, (iv) the obtained individual Zernike coefficients are finally averaged over the M neighboring positions. This spatial averaging reduces the maximal theoretical rate at which the phase can be extracted (typically to 2 to 3 Hz if the sample or the beam is moved fast and for $M = 5$). In our case, fast measurements were not required and therefore not performed (the sample was translated by a manual stage).

3. Results

3.1 Measuring known aberrations with CGWS in rat brain slices

In order to show that CGWS is able to measure aberrations *in vivo*, it is necessary to generate well-defined aberrations. The rat brain itself has some aberrations (that remain to be measured), but in order to assess the quality of our measurement, we have chosen to impose known aberrations and check that CGWS is able to measure them correctly. Previous work has shown that moving the position of the CG relatively to the AFP induces known aberrations [24]. This relative movement can either be produced by changing the length of the reference arm (Fig. 2(c)) or simply by index mismatch when focusing in a tissue with refractive index different than water (Fig. 2(b)). The two main aberrations introduced are defocus and 3rd order spherical aberration and their magnitude can be calculated exactly from the objective NA (Appendix A). Here, the following experiment is performed: (a) change the relative distance between the AFP and the CG for different depths in the rat brain; (b) calculate theoretically the expected aberrations, which are depth-independent (see Appendix A); (c) measure the aberrations experimentally with CGWS and compare them to the theoretical predictions. Since the sample can itself create some unknown amount of aberration, we do not represent the absolute magnitude of the aberrations but their slope as a function of the relative position between the AFP and the CG.

We observe that CGWS accurately measures the defocus slope at shallow depths for both objective pairs, since the measured slopes match the theoretical predictions (Figs. 4(a), 4(b), 4(d) and 4(e)). When going deeper in the tissue, however, the measured slope is always smaller than the theoretical prediction, and rapidly diminishes (see, e.g., Figs. 4(d) and 4(e)). The critical depth at which the drop occurs depends on the objective pair used. While for the $20\times/0.5$ objective we are able to measure the defocus down to $400 \mu\text{m}$ with little or no deviation, the accuracy degrades very much more quickly with the $63\times/0.9$ objective: at $300 \mu\text{m}$, we measure already only half of the expected slope and the measurement tends to a flat curve with a zero slope.

We also compare the 3rd order spherical aberration measured by CGWS to predictions (Figs. 4(c), 4(f) and 4(g)). For the $20\times/0.5$ objective, the expected spherical aberration slope is too small to be accurately measured by CGWS (it corresponds to a RMS wavefront error of $\lambda/162$ when the CG is displaced by $10 \mu\text{m}$). However, for the $63\times/0.9$ objective, the theoretical 3rd order spherical aberration is much larger and CGWS is able to measure it accurately. Not only is the slope for shallow AFP depths close to the theoretical prediction, but also the drop in the measured slope occurs approximately for the same depth as for the defocus (compare Figs. 4(e) and 4(g)).

Finally, let us note that aberrations could not be measured at very shallow depths, for the AFP between 0 and 40 μm . Even though our CV has an axial FWHM of only 7.9 μm , its shoulders pick up the strong reflection from the glass surface, which dominates the backscattering from the tissue at the center of the CV.

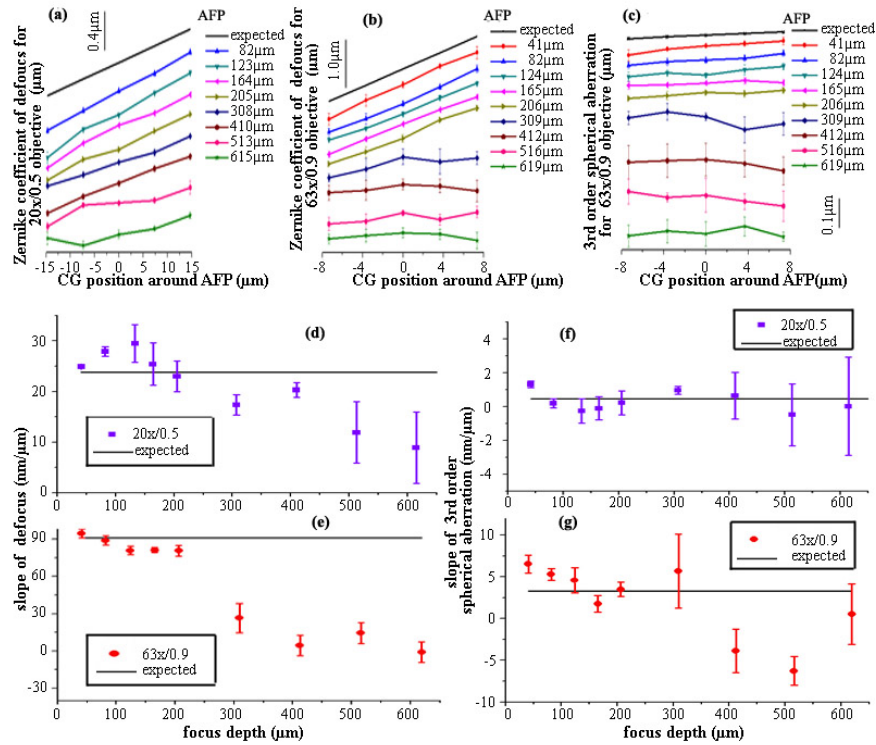


Fig. 4. Measuring known aberrations at different depth for the 20 \times /0.5 and the 63 \times /0.9 objectives. (a) and (b): raw defocus measurement at different depths as a function of CG position for respectively the 20 \times /0.5 and 63 \times /0.9 objectives and theoretical curves. (c): raw 3rd order spherical aberration measurement for the 63 \times /0.9 objective at different depths as a function of CG position. In (a), (b) and (c), curves were vertically shifted for visibility. (d) and (e): from subfigures (a) and (b), defocus slope as a function of depth for respectively the 20 \times /0.5 and 63 \times /0.9 objectives. (f) and (g): slope of the 3rd order spherical aberration and comparison with theory for respectively the 20 \times /0.5 objective and 63 \times /0.9 objective.

3.2 GCWS selects multiply scattered photons in rat brain slices

In order to understand what limits the maximum depth at which CGWS can be performed, we need a better understanding of the selection of photons by the CG as a function of the depth in the tissue. To get an insight into which photons actually fall within the CG and which information they carry about the wavefront of interest, we measure the speckle size and the magnitude of the CGWS signal at different depths for the two pairs of objectives (Fig. 5).

The speckle size, which is calculated as the FWHM of the autocovariance function of the electric field on the pupil [25], is the most important parameter to assess the size of the coherence-gated region. Assuming ballistic propagation to and from the CV and a random distribution of scatters within the CV, we expect the speckle size to depend on the CV extension. If the size of the CV is of the order of the extent of the point spread function (PSF) of the objective and if the CV lies around the AFP, scatters within CV cannot be resolved by the objective and produce therefore a wavefront without speckle. If the CV moves away from the AFP, or if the CV extends laterally (as when aberrations are present or when multiple scattering starts to be non-negligible), then we expect to see in the CGWS signal a speckle

structure, whose typical size is inversely proportional to the lateral extension of the CV. At the smallest depths, the size of the speckle is maximal when the defocus is minimal, as expected from the fact that the focus is the smallest at this position (Fig. 10 below).

Moreover, the speckle size also decreases monotonically with the depth in the tissue (Fig. 5(a), FOV 1000 μm and Fig. 5(b), FOV 530 μm). This can be interpreted as the fact that the effective coherent volume, from which selected photons seem to originate, is enlarged in depth by multiply scattering. We denote in the following this volume the “diffusive Coherence Volume” (dCV), which presumably is larger laterally than the CV and has an axial extension larger than the coherence length. Monte Carlo simulation have explored the spatial extent of this volume [26], but as exact scattering properties of the brain (in particular the anisotropy of the scattering) are still ill known, it is hard to predict the shape of this volume. The lateral extension of the dCV (d_{dCV}) (estimated from the typical size of the speckle in the objective pupil (d_{speckle}) by $d_{\text{dCV}} \approx 1.22 \lambda f_{\text{obj}} / d_{\text{speckle}}$ [27,28], where f_{obj} is the focal length of the objective) increases monotonically and seems to saturate at large depths (Fig. 5(c), FOV 1000 μm and Fig. 5(d), FOV 530 μm).

As the lateral extent of the dCV is several hundreds of μm at large depths, we checked whether the microscope FOV could limit the dCV and alter the CGWS measurement. When the CGWS system works, the FD (Fig. 1) is totally opened and it corresponds to the maximal microscope FOV (1000 μm and 530 μm for 20 \times /0.5 and for 63 \times /0.9 objectives respectively). By closing the FD, we measured the speckle size for several values of the FOV, calculated the corresponding dCV size (Figs. 5(a), 5(b), 5(c) and 5(d)) and computed the defocus slope to determine the FD range for which aberrations can still be estimated (Figs. 5(e) and 5(f)). As the FD is placed in the detection arm, it does not influence the geometry of photon trajectories entering in the sample. However, a photon exiting the sample with a large angle (as if arising from a point outside the FOV) is blocked by the FD. Multiply scattered photons selected by the CGWS gate can therefore be rejected by the FD. Closing the FD reduces the maximum dCV extension reached at large depth (Figs. 5(c) and 5(d)): some scattered photons in the dCV are blocked by the FD. This effect is present at large depths where multiply scattered photons contribute to CGWS signal. But perturbation of dCV by the FD is progressive and it can already be seen at depths smaller than the mean free path, (about 200 μm in the cortex of adult rat in the far red [29–31]). The filtering of multiply scattered photons entering the CGWS gate by the FD is not precluding the correct estimation of the defocus slope (Figs. 5(e) and 5(f)), except for the very small range of FD size (FOV smaller than 180 μm (20 \times /0.5 objective) or than 60 μm (63 \times /0.9 objective). Above these FOV, the maximal depth at which defocus slope is correctly measured is the same for all FOV. These curves show that the setup FOV doesn't determine the maximal depth of the CGWS measurement.

The effect of the depth on the CGWS signal is also an interesting parameter. In classical ff-OCT, the drop in signal is expected to follow the exponential attenuation of the ballistic light from Beer-Lambert's law on a length scale given by half (because the light scattered at the focus travels twice the depth before exiting the sample) the mean free path (~ 100 μm in rat brain). In Figs. 5(g) and 5(h), we represent the magnitude of CGWS signal as its total integrated intensity. The signal increases first until a depth of about 100 to 150 μm and then decays slowly with a characteristic length scale larger than half the mean free path (700 μm for 20 \times /0.5 objective, 250 μm for the 63 \times /0.9 objective). This dependence of the CGWS signal on depth could be accounted for by the selection within the coherence gate of a large fraction of snake-like multiply scattered photons. This confirms that the CGWS signal is influenced by multiply scattered photons in rat brain tissue.

A possible explanation of the failure of CGWS at large depth could be that the speckle structure of the wavefront could not be resolved anymore at large depths by the camera pixels. To address this issue, we analyzed the wavefront at the maximal depths of measurement for each objective while binning the pixels of the camera (Fig. 6) before using the vSHS. We observe that for both objectives the defocus slope is still reliably measured, as long as there is

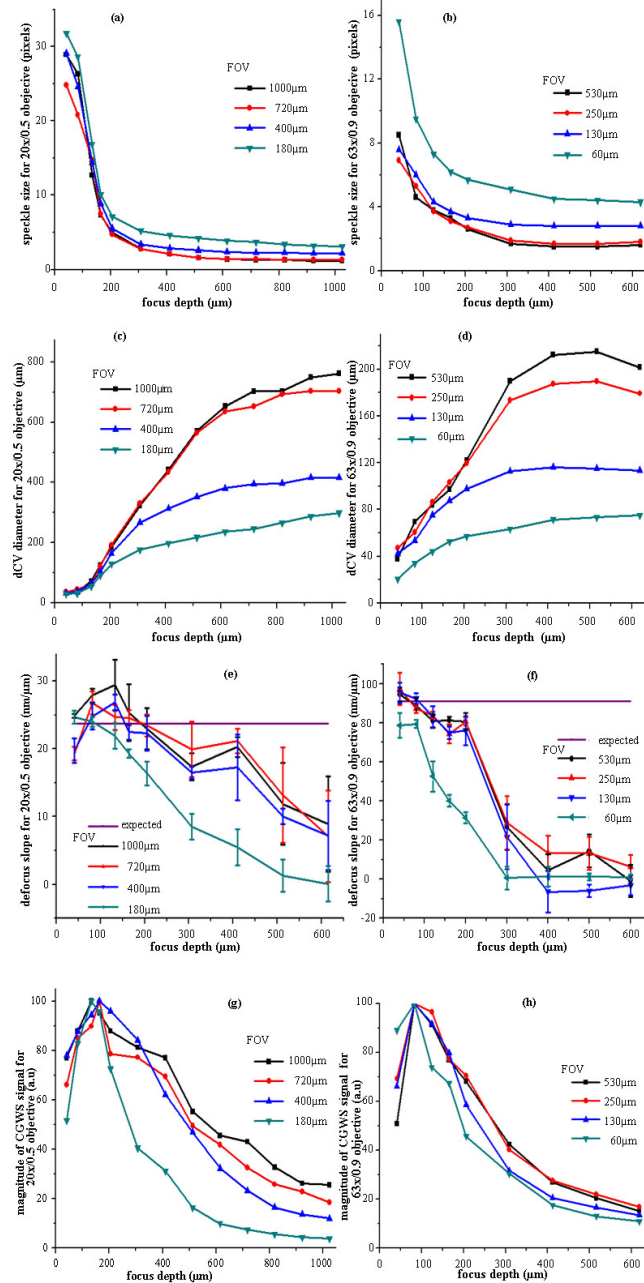


Fig. 5. Transition from single scattering to multiple scattering in CGWS measurement within rat brain slices (male Wistar, 45 days old.) and influence of the microscope FOV. (a) and (b) Speckle size as a function of depth when CG is centered on AFP. (c) and (d) dCV lateral extension estimated from the speckle size as a function of depth when CG is centered on AFP. (e) and (f) Defocus slope as a function of depth. (g) and (h) The magnitude of CGWS signal as a function of the depth. (a), (c), (e) and (g): 20×/0.5 objective; (b), (d), (f) and (h) 63×/0.9 objective. In each panel, the measurements are shown for four different FOV corresponding to four different diameters of the FD.

at least about 1.2 to 1.3 pixels per speckle on average. As the speckle size for both objectives is larger than 2 pixels at the critical depths where the wavefront measurement fails, this shows that the CGWS measurement is not limited by the camera sampling in our setup.

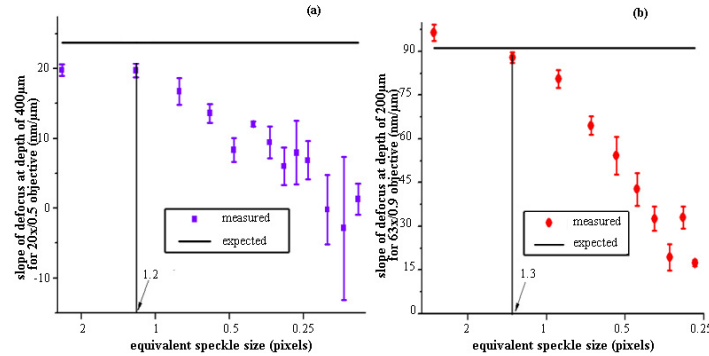


Fig. 6. Influence of speckle sampling by the camera pixels on the CGWS measurement (wavefront obtained by averaging $M = 40$ positions). The slope of defocus is plotted at depths of $400\ \mu\text{m}$ (a) and $200\ \mu\text{m}$ (b) for respectively the $20\times/0.5$ and $63\times/0.9$ objectives as a function of the average number of pixels per grain of speckle, which was varied by binning the camera pixels before propagation through the vSHS (from left to right on the horizontal axis, the binning of the pixels is increased and therefore the speckle size in unit of pixels is decreased).

4. Discussion

Under the condition of single scattering regime, which is characterized by a ballistic transport to and from the CV and by a single backscattering event in CV, the wavefront distortions can be accurately measured by CGWS, as verified previously by [10–12]. We show in this paper, that for more strongly scattering structures such as the rat brain, multiple scattering starts playing a major role in CGWS. The photons selected by the temporal gate are not confined in the CV, but arise from a much larger volume referred to as the dCV.

The existence of an extended volume selected by temporal gating explains the CGWS performance as a function of depth. Due to multiple scattering, extra photons in the dCV participate in the wavefront measurement and the deeper in the sample, the larger the dCV. This effect (a) decreases the size of the speckle in the pupil (making the wavefront harder to measure) and most importantly (b) perturbs the wavefront itself, since it is averaged over photons coming from a much larger volume than CV.

Our main result is to demonstrate that the CGWS measurement of the known aberrations imposed in our experiment remains valid at large depths. CGWS could be performed indeed at depths much deeper than the depth at which only ballistic photons are selected by the CG. This result demonstrates the possibility to implement CGWS as wavefront sensor in a close loop system to improve microscopes working in scattering samples, such as two-photon microscopy or full-field OCT.

However, at depths larger than a critical depth, the CGWS fidelity drops. We have shown that this critical depth was neither due to a spatial filtering of the dCV due to a limited FOV of the microscope nor due to a poor sampling of the small speckle grain by the camera pixels. Therefore the maximal depth is more probably related to the fact that above the critical depth the wavefront averaged over all the photons in the dCV does not carry the same information as the one originating from the ballistic CV. A better understanding of this limit and of the fact that it depends on the objective used will need a model of scattering in the tissue [26].

It is interesting to compare CGWS with ff-OCT or conventional OCT. Our CGWS setup is mainly different in two aspects: the spatial coherence of the source plays a major role here and the coherence gating is performed directly in the pupil of high-NA objectives. In regular ff-OCT with thermal light, photons are indeed selected in the coherence window both based on their temporal and on their spatial position: the multiply scattered photons are mostly

eliminated. In the CGWS setup, we measure the interference pattern with the reference in the pupil of the objective: we therefore select photons based only on their path length (the temporal coherence). As a consequence the multiply scattered photons that fall within this temporal gate participate in CGWS, even if they have been notably deviated. This results in a temporal gating only of the backscattered photons. We therefore select much more photons that just the ballistic ones.

Finally, in the regime determined above, where known aberrations could be reliably measured (200 μm depth for the $63\times/0.9$ objective, 400 μm depth for the $20\times/0.5$ objective), PSFs are calculated from the wavefront measured by CGWS using the first 28 Zernike coefficients whose tilt and defocus are numerically removed (Fig. 7). It is calculated at the experimental CG positions where the defocus is minimal (but never exactly zero). We observe that the PSF degrades notably over the range of reliability of the CGWS. Some aberrations (mostly defocus and some amount of 3rd order spherical aberration) stem from the coherence gating itself, since the CG position was only close to the optimal defocus position. Other aberrations could have been introduced by the sample itself (as, e.g., 3rd order spherical aberration due to index mismatch [17]). However, these results have to be taken cautiously, in particular we cannot say anything about the isoplanatism of the aberrations as long as the wavefront we measured is not applied to correct a full-field image. However they give an estimate of the degradation of the image expected when going in depth in the sample.

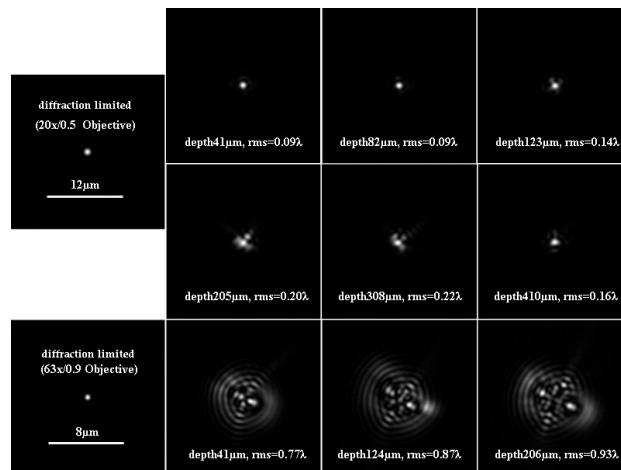


Fig. 7. Point Spread Function as extracted from the wavefront measured by CGWS for the minimal defocus position using the first 28 coefficients. The PSF was scaled over the whole gray values (0-255). We observe that the PSF degrades notably over the range of reliability of the CGWS.

5. Conclusion

We have implemented a new CGWS scheme based on a Linnik interferometer with a SLED as low temporal but high spatial coherence light source. Compared to the previous implementation of CGWS [10–12], its main technical advantages are the automatic compensation of dispersion between the two arms. Here the short coherence length for coherence gating is obtained from a broadband continuous source, with two symmetric arms to ensure that there is no phase delay between them for all wavelengths. Thanks to this simple design, a consequent advantage is his easy implementation on any microscope. Moreover, it offers in the future the possibility to modify easily the CGWS setup in terms, e.g., of its central wavelength or its coherence length.

In fresh rat brain slices, we successfully measured up to a depth of about 400 μm for a $20\times/0.5$ objective and 200 μm for a $63\times/0.9$ objective known aberrations, obtained by displacing the CG position with respect to the AFP in the sample. However, measurement of

the speckle size and the CGWS signal as a function of depth in the sample demonstrates that the CG was not successfully rejecting multiply scattered photons even at shallow depths. This was attributed to a large amount of multiply scattered photons, which could have similar time of flight in the sample as the photons of the reference arm. CGWS could be directly applicable at shallow depth or in thin slices, where regular wavefront sensing methods fail. It would allow the implementation of adaptive corrections. At larger depth, our results show that CGWS allows the quantitative measurement of known aberration despite the selection of a large amount of multiply scattered photons. Its benefits for close-loop adaptive optics have to be demonstrated by coupling it to any microscopy modality and by measuring the image improvement. Finally, imaging at large depth may require the improvement of the rejection of the multiply scattered photons, e.g., by the increase of the scattering length, e.g., by the use of higher-wavelength light [32,33].

Appendix A: Analytical computation under sine condition of the aberrations for a refractive-index-mismatch sample covered by a coverslip

For an objective operating under the sine-condition, an axial shift of the diffraction-limited focus corresponds to a defocus and to all orders of the spherical aberrations [34]. Binding et al. have proposed a concise formula to predict the aberrations for the mismatched index situation taking into account the spread between the NFP and AFP [17]. Here, we derive the analytical aberrations when a cover slip is inserted between the sample and the immersion water, as it is the case in most *in vivo* recordings when a glass coverslip is used to stabilize the brain after exposing it through a craniotomy.

Under the sine condition, the principal surface of the objective corresponds to a sphere segment of radius $n_i f$ (Fig. 8) [35]. To determine the wavefront from a point A (i.e., the single pass aberrations) on the optical axis, we imagine a point source at this position and trace its rays into the back focal plane (BFP) of the objective. Ray tracing restricted to the meridional plane is sufficient because of rotational symmetry.

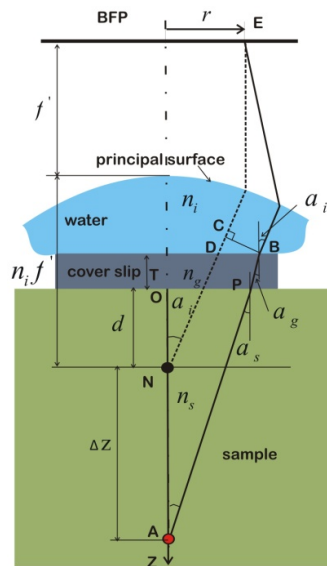


Fig. 8. Geometry of schematic for ray tracing. Refractive index of water, glass slip, and sample are n_i , n_g , n_s respectively. If the sample was a pure water solution and if there was no coverslip, the focus in this aberration free case would be located at the position N on the optical axis. The origin O is located at the cross point of the optical axis to the second surface of the glass coverslip, the Z axis is defined along the optical axis OA with the positive direction pointing towards the sample (away from objective). The distance ON is noted d , the thickness of the glass coverslip T , the actual point source is A and the distance AN is noted Δz .

Emanating from A at an angle α_s with respect to OA, a ray is refracted and crosses the coverslip surfaces at P and B. The refraction angles in the glass coverslip and in the immersion water are α_g and α_i respectively. It crosses the BFP at E (at a distance r of the optical axis OZ). An auxiliary line BC is drawn perpendicular to the ray NC emanating from the NFP (N) at an angle α_i with respect to OA. According to Fermat's Principle, all rays of a planar wavefront transmitted through the objective have the same optical path length when they reach their common focusing point in the BFP. Thus all the rays at an angle α_i with respect to OZ in water arrive at point E, which is at a distance $r=n_i f \sin \alpha_i$ of OZ on the BFP.

For the light emanating from the NFP N in the aberration free case, a spherical wavefront will be produced at the principal surface, which corresponds to a planar one at the BFP. The optical path difference $W(r)$ between the rays originating from A (in the presence of sample and coverslip) and from N (in the aberration-free case, i.e., in the absence of sample and coverslip, with the full light path in water) and reaching the BFP in E, is equal to the optical path from A to B minus the optical path from N to C.

The optical path from A to B is

$$OP(A) = n_s AP + n_g PB = n_s (d + \Delta z) / \cos \alpha_s + n_g T / \cos \alpha_g. \quad (\text{A.1})$$

The optical path from N to C is

$$OP(N) = n_i NC = n_i [(d + T) / \cos \alpha_i + BD \sin \alpha_i], \quad (\text{A.2})$$

where $BD = (d + \Delta z) \tan \alpha_s + T \tan \alpha_g - (d + T) \tan \alpha_i$. Thus $W(r)$ is

$$W(r) = (d + \Delta z)(n_s^2 - N_r^2)^{1/2} + T(n_g^2 - N_r^2)^{1/2} - (d + T)(n_i^2 - N_r^2)^{1/2}, \quad (\text{A.3})$$

where $N_r = r/f$ is the relative numerical aperture of the rays reaching E in the BFP. Suppose the objective illuminated with a Gaussian intensity profile has an effective numerical aperture eNA (\leq NA, see below) corresponding to a radius of the effective pupil r_0 in the BFP plane and an effective entrance angle α_0 , the relative numerical aperture could be then normalized as $N_r = r/r_0$ eNA = $\sin \alpha_i / \sin \alpha_0$ eNA. If $T=0$, then $W(r) = (d + \Delta z)(n_s^2 - N_r^2)^{1/2} - d(n_i^2 - N_r^2)^{1/2}$, which is the same as [17]. If $T=0$ and $n_s=n_i$, $W(r) = \Delta z(n_s^2 - N_r^2)^{1/2}$, as in [36–38].

Analytical Zernike coefficients can be computed by expanding $W(r)$ into a series of Zernike modes by numerical convolution with the individual Zernike polynomials [21]. The AFP is defined as the position where the Zernike defocus is 0. For an objective that meets sine condition, all rotationally symmetric aberrations such as defocus, third order spherical aberration vary with CG position even when no actual aberrations are present [10]. When the CG position is moved with respect to the AFP, Eq. (A.3) is used to compute the Zernike defocus and the Zernike 3rd order spherical aberration as a function of CG position. The theoretical slopes of these curves are found to be constant (within 0.2% variation in the ranges of depths and CG position studied).

The aberrations created by moving the CG depend on the effective NA (eNA) of the objective illuminated with a Gaussian intensity profile. eNA was defined as the equivalent NA of an objective of same focal length illuminated with a constant intensity profile and providing the same in-plane resolution. For an objective of pupil diameter D_t , illuminated with a Gaussian beam of diameter D_b (measured at $1/e^2$), the truncation ratio t is defined as $t = D_b/D_t$. Using [31], the 20×/0.5 objective (truncation ratio 1.22) has an eNA of 0.47 and the 63×/0.9 objective (truncation ratio 1.44) has an eNA of 0.85.

Appendix B: Supplementary Information

B.1. CGWS setup

The components used are: a SLED light source (center wavelength 750 nm, 1.2 mW, FWHM bandwidth 23 nm) coupled to a single mode fiber (NA = 0.11, EXS7505-841, Exalos, Swiss) with a collimator of focal length 10 mm, AC080-010-B; Thorlabs, US); a polarizer Pol (NT47-603; Edmund Optics, US) and a $\frac{1}{4}$ waveplate (AHWP05M-980; Thorlabs, US); beam expander (5x Zoom, BE02-05-B; Thorlabs, US); L1 ($f = 150$ mm, G322352525, Linos, Germany), L2 ($f = 200$ mm, G322353525, Linos, Germany); non-polarizing beam splitters BS1 and BS2 (50:50, BS014; Thorlabs, US); reference and sample arm pair of objectives (20 \times /0.5W, UPlanFI; Olympus) or (63 \times /0.9 W, HCX APO, Leica); a tilted coverslip identical to the one covering the sample to balance dispersion; a Piezo actuator PZT (resonant frequency 138 kHz, range 9.1 ± 1.5 μm , AE0505D08; Thorlabs, US) with a silicon mirror M (with low reflectivity in reference arm to improve the contrast of interference pattern) mounted on it; motorized linear translation stages TS1 and TS2 (range 28 mm, T-LS28-M; Zaber, Canada); a field adjustable diaphragm; a CCD camera CCD2 conjugated to the objective focus (resolution 1024 \times 1024, pixel size 14 $\mu\text{m} \times 14$ μm , pixel depth 12 bits, DS11-01M15, Dalsa, Canada); a CCD camera CCD1 (resolution 1024 \times 1024, pixel size 12 $\mu\text{m} \times 12$ μm , pixel depth 12 bits, DS-21-01M60-12E, Dalsa, Canada). The pupil apertures of the both objectives are conjugated to the active surface of CCD1 by L1 and L2.

The beam dimensions are the following. The collimated beam of the SLED is circularly polarized after Pol and QWP. Before entering the interferometer, the beam is expanded to 11 mm ($1/e^2$ width) by the beam expander, so that the objective pupils are overfilled by a factor of 1.22 for the 20 \times /0.5 objective and 1.92 for the 63 \times /0.9 objective. The diameter of the objective pupils imaged on CCD1 (12 mm for the 20 \times /0.5 objective and 7.62 mm for the 63 \times /0.9 objective) are smaller than the sensitive surface of CCD1 (12.28 mm \times 12.28 mm).

B.2. CGWS Calibration

We calibrated the CGWS with a real SHS (HASO 3, Imagine Optic) using a mirror as sample and with the 20 \times /0.5 objective. By displacing the mirror along the microscope axis, we introduced a shift of twice the mirror displacement and the defocus aberration at each position was recorded both with SHS and CGWS. Both the SHS and CGWS correctly measured the slope of Zernike defocus and were in good agreement with the theoretical one (Fig. 9). The measured Zernike defocus coefficient of SHS has been normalized in the standard (Noll) notation [21].

CGWS may report erroneous astigmatism (depending on the size of the scatters) if linearly polarized light is used [10], and these errors can be avoided by the use of circularly polarized light. Our setup, therefore, contains a quarter wave-plate in the sample arm (Fig. 1) to ensure

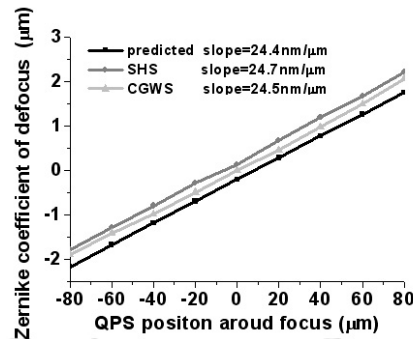


Fig. 9. CGWS calibration. Measured defocus slope with SHS and CGWS compared to the predicted curve (for $e\text{NA} = 0.47$ using the 20 \times /0.5 objective).

that the sample was illuminated by circularly polarized light. We checked in this case that spurious astigmatism disappeared, thus demonstrating that no alignment-induced astigmatism was present in our system (data not shown).

B.3. Animal preparation

All surgical procedures were in accordance with the European Community guidelines on the care and use of animals (directive 86/609/CEE, CE official journal L358, 18th December 1986), French legislation (décret 97/748, 19th October 1987, J. O. République française, 20th October 1987), and the recommendations of the CNRS.

Before surgery, the rat was anesthetized by urethane injection (1.5 g/kg). Supplementary dose of urethane was applied if necessary. The brain was taken out, put into the solution (NaCl: 150 mMol/L, KCl: 2,5 mMol/L, Hepes: 10 mMol/L pH = 7.4) and could be stored for 3 days at most in 4°C refrigerator. For CGWS measurement, the brain was sliced, then held on a glass slip, and covered with a cover slip to protect it. During the experiments, the slice was always immersed in the solution and the experiment lasted less than 3 hours.

B.4. Speckle dimension as a function of CG position at shallow depth

At the smallest depths, the size of the speckle is maximal when the defocus is minimal, as expected from the fact that the focus is the smallest at this position (Fig. 10).

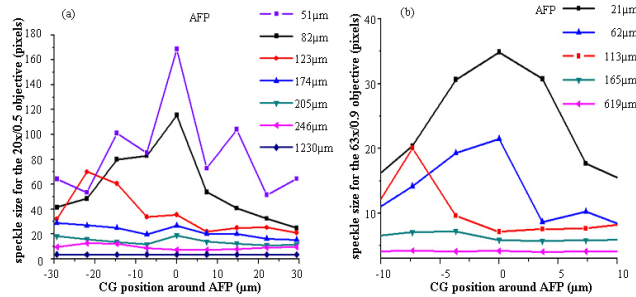


Fig. 10. Speckle size as a function of the CG position relative to the AFP for different depths for the 20x/0.5 (a) and the 63x/0.9 (b) objectives.

Acknowledgments

This work was supported by ANR RIB grants MICADO no. ANR-07-RIB-010-02 and ANR-07-RIB-010-04. J. B. and J. W. were funded by the Foundation Pierre-Gilles de Gennes. We thank LLTech for the use of the LightCT software. We are grateful to Winfried Denk, who allowed us to use the phase reconstruction algorithm implemented in his group.